ARTICLES
https://doi.org/10.1038/s41561-022-00978-3

nature geoscience

Check for updates

Sustained mid-Pliocene warmth led to deep water formation in the North Pacific

H. L. Ford[1,2] ✉, N. J. Burls[3], P. Jacobs[4,5], A. Jahn[6], R. P. Caballero-Gill[3], D. A. Hodell[2] and A. V. Fedorov[7]

Geologic intervals of sustained warmth such as the mid-Pliocene Warm Period can inform our understanding of future climate change, including the long-term consequences of oceanic uptake of anthropogenic carbon. Here we generate carbon isotope records and synthesize existing records to reconstruct the position of water masses and determine circulation patterns in the deep Pacific Ocean. We show that the mid-depth carbon isotope gradient in the North Pacific was reversed during the mid-Pliocene compared with today, which implies water flowed from north to south and deep water probably formed in the subarctic North Pacific Deep Water. An isotopically enabled climate model that simulates this North Pacific Deep Water reproduces a similar carbon isotope pattern. Modelled levels of dissolved inorganic carbon content in the North Pacific decrease slightly, although the amount of carbon stored in the ocean actually increases by 1.6% relative to modern due to an increase in dissolved inorganic carbon in the surface ocean. Although the modelled Pliocene ocean maintains a carbon budget similar to the present, the change in deep ocean circulation configuration causes pronounced downstream changes in biogeochemistry.

The ocean is the largest reservoir of exchangeable carbon in the climate system (~38,000 petagrams carbon (PgC)) and has absorbed approximately a third of anthropogenic carbon emissions[1]. So far, most of this anthropogenic carbon has been absorbed in the upper 700 m of the water column, but there are broad implications for the role of deep ocean circulation in future long-term carbon storage. The deep arm of the meridional overturning circulation moves water masses along the ocean depths, and as these waters age they accumulate dissolved inorganic carbon (DIC)[2]. The North Pacific acts as an area of carbon storage because it is at the end of the 'global conveyor belt' and contains a large amount of DIC. Currently, no deep water formation occurs in the North Pacific because of a strong halocline that prevents deep convection[3]. However, proxy and modelling results suggest that North Pacific deep water formation may have occurred during past warm periods, potentially impacting the ocean's ability to store carbon[4–8].

The mid-Piacenzian stage of the Pliocene epoch (3.264–3.025 million years ago (Ma)), often referred to as the mid-Pliocene Warm Period, is an age of sustained warmth, with the global mean surface temperature estimated at 2–3 °C above pre-industrial temperature and atmospheric CO_2 (350–400 ppmv) similar to current anthropogenic levels[9–11]. As it is a potential analogue for future climate change, there are intense efforts to characterize the mid-Piacenzian through proxy reconstructions and modelling[11]. Many modelling efforts fail to simulate the magnitude of polar amplification and the reduced meridional temperature gradient implied by the proxy reconstructions[12]. As the meridional temperature gradient is tightly coupled to atmospheric heat and water-vapour transport, this limitation affects our understanding of climate dynamics necessary to sustain global warmth[13–15].

In a modelling experiment that alters cloud albedo to simulate a reduced meridional temperature gradient comparable to Pliocene reconstructions, a reduction in northward atmospheric water-vapour transport eroded the North Pacific halocline[4]. Subsequently, the weakened upper-ocean stratification in the subarctic North Pacific enabled active ocean ventilation and deep water formation. Importantly, the model ran for ~3,000 simulation years to allow for the deep ocean to adjust to the Pliocene forcing, and the Pacific meridional overturning circulation (PMOC) fully appeared only ~1,500 years into the simulation; many climate models are run for ~500–1,000 years, which is not enough time for the deep ocean to fully equilibrate.

For this study we present stable isotope data and compile existing records from the Pacific Ocean to reconstruct deep ocean water masses and investigate the spatial extent of a Pliocene PMOC. We compare this $\delta^{13}C$ synthesis with an isotopically enabled climate model (Community Earth System Model (CESM); Methods) and show good proxy and model agreement in support of the formation of North Pacific Deep Water (NPDW) during the mid-Pliocene Warm Period. Because of NPDW formation, the DIC concentration decreases in the deep Pacific and increases in the surface ocean, with possible biogeochemically cascading effects such as increased productivity and altered biogeochemical cycles in the eastern equatorial Pacific[16,17]. Overall, there is little modelled change in global carbon storage during the mid-Pliocene Warm Period.

Mapping North Pacific circulation with carbon isotopes

Carbon isotopes of DIC ($\delta^{13}C_{DIC}$) trace water-mass circulation in the modern ocean. The $\delta^{13}C$ of benthic foraminifera shells, which is a proxy for $\delta^{13}C_{DIC}$, can be used to reconstruct water-mass circulation in the past[18–20]. The ability to trace water masses using $\delta^{13}C$ reflects the fact that biological and physical formation processes create different $\delta^{13}C$ 'endmembers' where water masses form today. That is, the $\delta^{13}C$ values in the surface source areas for deep water formation in the North Atlantic and Southern Ocean are different enough

[1]School of Geography, Queen Mary University of London, London, UK. [2]Godwin Laboratory for Palaeoclimate Research, Department of Earth Sciences, University of Cambridge, Cambridge, UK. [3]Department of Atmospheric, Oceanic and Earth Sciences, George Mason University, Fairfax, VA, USA. [4]Department of Environmental Science and Policy, George Mason University, Fairfax, VA, USA. [5]NASA Goddard Space Flight Center, Greenbelt, MD, USA. [6]Department of Atmospheric and Oceanic Sciences and Institute of Arctic and Alpine Research, University of Colorado Boulder, Boulder, CO, USA. [7]Department of Earth and Planetary Sciences, Yale University, New Haven, CT, USA. ✉e-mail: h.ford@qmul.ac.uk

Table 1 | Site information, including site name, longitude, latitude and bottom water depth (m)

				Pre-industrial water column[a]		Late Holocene		Mid-Piacenzian[b] (3.264–3.025 Ma)					
Site name	Longitude	Latitude	Water depth (m)	Water-column $\delta^{13}C$	Water-column OC3 search	Core-top $\delta^{13}C$	Core-top OC3 search	Benthic $\delta^{13}C$	$\delta^{13}C$ s.d.	N	Water-column anomaly[c]	Core-top anomaly	Reference[d]
ODP1018	123.3° W	37.0° N	2,477	−0.126	$\Delta d=1{,}000$ km, $\Delta z=z/5$	0.060	$\Delta d=500$ km, $\Delta z=z/10$	−0.168	0.16	5	−0.042	−0.228	5
ODP1208	158.2° E	36.1° N	3,346	0.059	$\Delta d=1{,}000$ km, $\Delta z=z/5$	0.212	$\Delta d=2{,}000$ km, $\Delta z=z/5$	−0.040	0.23	160	−0.099	−0.252	31
ODP1014	120.0° W	32.8° N	1,165	−0.311	$\Delta d=500$ km, $\Delta z=z/10$	−0.062	$\Delta d=500$ km, $\Delta z=z/10$	−0.136	0.13	7	0.175	−0.074	5
ODP1209	158.5° E	32.7° N	2,387	−0.152	$\Delta d=1{,}000$ km, $\Delta z=z/5$	0.099	$\Delta d=2{,}500$ km, $\Delta z=z/5$	0.025	0.17	61	0.177	−0.074	this study
ODP1210	158.3° E	32.2° N	2,574	0.000	$\Delta d=500$ km, $\Delta z=z/10$	0.178	$\Delta d=2{,}000$ km, $\Delta z=z/5$	0.026	0.22	40	0.026	−0.152	this study
ODP1148	116.6° E	18.8° N	3,294	0.180	$\Delta d=2{,}000$ km, $\Delta z=z/5$	0.324	$\Delta d=500$ km, $\Delta z=z/10$	−0.410	0.49	19	−0.590	−0.734	23
ODP1143	113.3° E	9.4° N	2,772	0.145	$\Delta d=1{,}500$ km, $\Delta z=z/5$	0.130	$\Delta d=500$ km, $\Delta z=z/10$	0.040	0.38	97	−0.105	−0.090	25
ODP1241	86.4° W	5.8° N	2,027	−0.248	$\Delta d=2{,}000$ km, $\Delta z=z/5$	0.210	$\Delta d=500$ km, $\Delta z=z/10$	−0.170	0.19	70	0.078	−0.380	30
ODP806	159.4° E	0.3° N	2,520	0.017	$\Delta d=1{,}000$ km, $\Delta z=z/5$	0.265	$\Delta d=500$ km, $\Delta z=z/10$	0.160	0.19	71	0.143	−0.105	28
ODP849	110.5° W	0.2° N	3,839	0.115	$\Delta d=500$ km, $\Delta z=z/10$	0.271	$\Delta d=500$ km, $\Delta z=z/10$	−0.020	0.30	68	−0.135	−0.291	24
DSDP586	158.5° E	0.5° S	2,208	0.035	$\Delta d=1{,}000$ km, $\Delta z=z/5$	0.399	$\Delta d=500$ km, $\Delta z=z/10$	−0.030	0.07	4	−0.065	−0.429	26
ODP1239	82.1° W	0.7° S	1,414	−0.102	$\Delta d=500$ km, $\Delta z=z/10$	0.407	$\Delta d=500$ km, $\Delta z=z/10$	−0.330	0.25	118	−0.228	−0.737	30
ODP846	90.8° W	3.1° S	3,296	−0.144	$\Delta d=1{,}000$ km, $\Delta z=z/5$	0.127	$\Delta d=1{,}000$ km, $\Delta z=z/5$	−0.160	0.27	100	−0.016	−0.287	32
DSDP593	167.7° E	40.5° S	1,088	0.787	$\Delta d=1{,}000$ km, $\Delta z=z/5$	1.114	$\Delta d=1{,}000$ km, $\Delta z=z/5$	0.820	0.11	17	0.033	−0.294	29
ODP1123	171.5° W	41.8° S	3,290	0.388	$\Delta d=500$ km, $\Delta z=z/10$	0.445	$\Delta d=500$ km, $\Delta z=z/10$	0.266	0.24	63	−0.121	−0.179	43
ODP1125	177.6° W	42.5° S	1,365	0.720	$\Delta d=500$ km, $\Delta z=z/10$	0.643	$\Delta d=500$ km, $\Delta z=z/10$	−0.650	0.18	117	−1.370	−1.293	27
DSDP594	175.0° E	45.7° S	1,204	0.998	$\Delta d=1{,}000$ km, $\Delta z=z/5$	0.949	$\Delta d=500$ km, $\Delta z=z/10$	0.100	0.44	70	−0.898	−0.849	27
U1338	118.0° W	2.51° N	4,200	0.150	$\Delta d=1{,}000$ km, $\Delta z=z/5$	0.170	$\Delta d=1{,}000$ km, $\Delta z=z/5$	−0.100	0.28	43	−0.250	−0.270	44

The change (Δ) in horizontal great-circle distance (Δd) and the vertical distance (Δz). [a]OC3 data, including pre-industrial $\delta^{13}C$ natural ocean water-column bottle data and late Holocene $\delta^{13}C$ from the benthic foraminifera genus *Cibicides* with the relevant search parameters for each site. [b]Mid-Pliocene (mid-Piacenzian) Warm Period $\delta^{13}C$ values, s.d. and number of data points within the interval. [c]Calculated anomaly (mid-Pliocene Warm Period minus pre-industrial/late Holocene). [d]References used in the compilation.

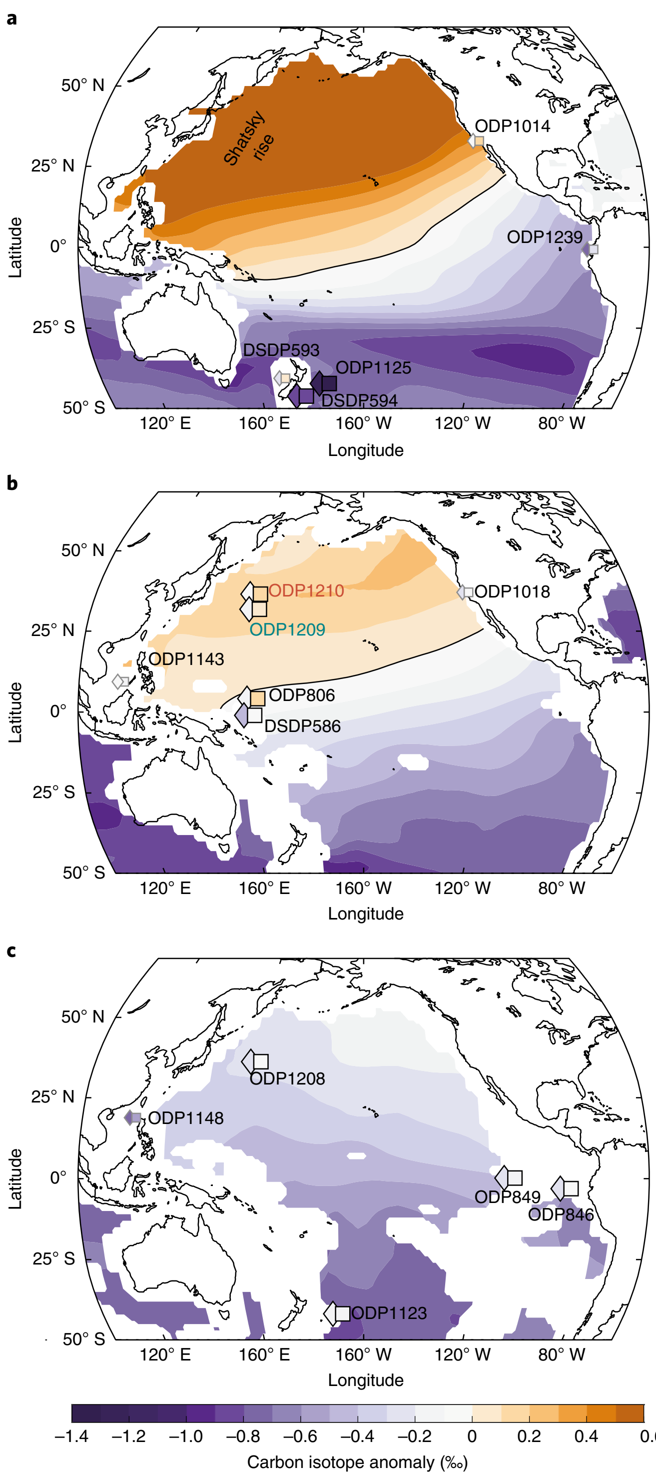

Fig. 1 | Reconstructed benthic $\delta^{13}C$ and modelled anomalies for the mid-Pliocene Warm Period. The benthic $\delta^{13}C$ anomaly (‰) is calculated from the OC3 database[20] with late Holocene core-top (diamonds) and modern $\delta^{13}C$ ocean-water (squares) values. Symbols for open ocean sites are large and outlined in black; symbols for marginal sites possibly influenced by boundary effects are small and outlined in grey. **a–c**, Horizontal basin-wide $\delta^{13}C$ anomalies for 1,000–1,500 m (**a**), 2,200–2,800 m (**b**) and 3,200–4,000 m (**c**) water depths. The largest anomaly is found in the west due to a deep western boundary current (for example, ref. [4]) related to western intensification of ocean circulation.

from one another to monitor a water mass sinking and moving through the ocean's basins.

In the modern ocean, North Atlantic Deep Water has a positive $\delta^{13}C$ value (~+0.6) and Antarctic Bottom Water has a negative $\delta^{13}C$ value (~−0.2) (ref. [21]). As these water masses traverse the ocean depths, they accumulate respired carbon and become more negative in their $\delta^{13}C$ values. The most negative $\delta^{13}C$ water mass is Pacific Deep Water (~−0.3 (ref.[19])), originally sourced from the South Pacific as a mixture of North Atlantic Deep Water, Antarctic Intermediate Water (AAIW) and Antarctic Bottom Water, which reflects the long circulation pathway and respiration of organic carbon.

Shatsky Rise is ideally positioned to monitor changes in North Pacific deep ocean circulation. In the northwest Pacific Ocean, Shatsky Rise is proximate to the western intensification of surface ocean currents[22], and multiple Ocean Drilling Program (ODP) sites on this bathymetric high allow for a near vertical depth transect of deep Pacific waters. Correlating our $\delta^{18}O$ records (Extended Data Fig. 1) with reference curves (for example, global benthic $\delta^{18}O$ stack Prob-stack) demonstrates good stratigraphic coverage of the middle Pliocene and permits identification of the mid-Pliocene Warm Period at ODP Sites 1209 and 1210 (2,387 and 2,574 m water depth, respectively).

Our $\delta^{13}C$ data (Extended Data Fig. 1), when combined with previously published records[5,23–32] (Table 1 and Supplementary Data 1), permit us to reconstruct mean intermediate and deep ocean circulation in the Pacific during the mid-Pliocene Warm Period (Figs. 1 and 2). Undoubtedly, there is $\delta^{13}C$ variability within the mid-Pliocene Warm Period owing to glacial–interglacial cycles and other sources, but the age model quality and $\delta^{13}C$ resolution of some sites does not allow us to characterize this variability without forgoing spatial coverage. Although some of the sites included are from continental margins (for example, California Margin) and marginal seas (for example, South China Sea) that may be influenced by boundary effects (for example, ref. [20]) (Fig. 1), we include all the available data here for completeness. Taking this into consideration, large symbols for open ocean sites are outlined in black, while those possibly influenced by boundary effects are small and outlined in grey. Shatsky Rise is in the open ocean, and productivity during the mid-Pliocene Warm Period was low[33–35], as it is today, so the lowering of $\delta^{13}C$ of epibenthic foraminifera resulting from a phytodetritus layer should not be an issue (Mackensen et al., 1993).

We calculated a pre-industrial anomaly by subtracting nearby Ocean Circulation and Carbon Cycling (OC3) late Holocene sediment and modern water-column $\delta^{13}C$ values[20] from the mid-Pliocene values (Table 1 and Supplementary Data 1). These anomaly maps (Figs. 1 and 2, sediment in diamonds and modern $\delta^{13}C$ ocean water in squares) show a pattern with positive $\delta^{13}C$ anomaly values in the North Pacific and negative $\delta^{13}C$ anomaly values in the South Pacific. These $\delta^{13}C$ anomaly patterns suggest changes in PMOC related to changes in water-mass formation distribution (where a water mass forms), character (how biological processes influence $\delta^{13}C$) and/or ventilation (how quickly the ocean overturns).

The positive $\delta^{13}C$ anomaly in the North Pacific between the Pliocene and late Holocene time slices suggests mid-Pliocene NPDW existed as a mid-depth water mass (core at ~1,500 m), similar to modern North Atlantic Deep Water. High $CaCO_3$ and opal accumulation and preservation in the subarctic North Pacific (Fig. 3) also supports younger ventilation ages in the deep ocean[4]. In the modern ocean, the North Pacific has little to no $CaCO_3$ preservation owing to old, acidic water, while opal is undersaturated, accumulating only in areas underlying deep convection (coastal upwelling, Southern Ocean) where the rain rate is high. Our Pliocene reconstructions (Figs. 1 and 2) indicate that NPDW extended to the Equator where it met AAIW. AAIW has a negative $\delta^{13}C$ anomaly that probably reflects changes in the $\delta^{13}C$ of this Southern Ocean endmember, which may be better constrained in the future by new

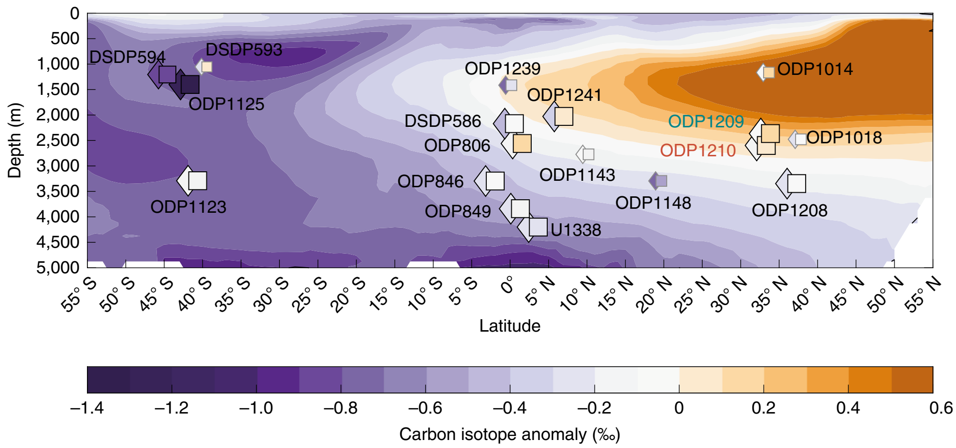

Fig. 2 | Observed benthic δ[13]C and modelled zonal-mean anomalies for the mid-Pliocene Warm Period. The vertical cross section across the Pacific shows the core and spatial extent of the PMOC.

records from recently completed International Ocean Discovery Program cruises.

Modelling NPDW formation

In two fully coupled climate simulations forced with changes in cloud radiative properties that give rise to large-scale warming patterns resembling Pliocene reconstructions, NPDW formation and a PMOC appear once the deep ocean starts to equilibrate, between ~500 and 1,500 years into the simulation. The imposed modifications in cloud radiative properties support reduced meridional and zonal sea surface temperature (SST) patterns resembling that of the early and mid-Pliocene (mid-Piacenzian) SST reconstructions, respectively, which are challenging to simulate using standard modelling methods[9,36], particularly with respect to the reduced gradients of the early Pliocene (Extended Data Fig. 2). Both simulations are performed with the CESM with active biogeochemistry[37] and carbon isotopes[38].

These simulations produce a strong and weak PMOC, respectively, and illustrate the impact of changing Pliocene SST gradients on the hydrological cycle and NPDW formation. The early Pliocene-like simulation is configured similarly to that of ref. [4], who described how changes in the hydrological cycle in response to Pliocene SST patterns led to the erosion of the North Pacific halocline, forming NPDW and a PMOC. The mid-Pliocene-like simulation is configured to align more with mid-Pliocene SST reconstructions (Methods and Extended Data Fig. 2). Although these simulations are similar to those of ref. [4], both simulations are now geochemically enabled and include carbon isotopes to facilitate a pair-wise comparison with benthic foraminifera δ[13]C values. The large-scale warming patterns and the associated hydrological cycle responses give rise to surface ocean buoyancy changes that drive weak (strong) PMOC cells within the mid-(early) Pliocene-like experiments. We present both experiments because $CaCO_3$ preservation records (Fig. 3) from the subarctic North Pacific suggest that the depth of NPDW formation (and therefore probably PMOC strength) fluctuated throughout the Pliocene[4], probably in response to variations in SST and density gradients.

The impact of a PMOC on $\delta^{13}C_{DIC}$ in both simulations shows spatial similarity with the reconstructed Pacific δ[13]C benthic foraminifera values (Figs. 1 and 2 and Extended Data Fig. 3), but the weaker PMOC that develops in the mid-Pliocene-like simulation aligns more closely with the reconstructed mid-Piacenzian δ[13]C values. Looking at the zonal mean (Fig. 2), the δ[13]C data largely correspond with the simulated changes (contours) in the age of each water mass, with the PMOC leading to a tongue of younger water centred at about 1,500 m, penetrating to about 3,500 m depth, and extending southward from a maximum δ[13]C value near 50° N (ref. [4]). For the abyssal North Pacific, however, ages increase relative to pre-industrial control values.

Horizontal basin-wide cross sections at 1,000–1,500, 2,200–2,800 and 3,200–4,000 m reveal a remarkably good correspondence (particularly when focusing on the sites less likely to be influenced by boundary effects) between the spatial patterns in the data and those simulated by the model in response to the presence of a PMOC (Fig. 1). These cross sections have an east–west structure in modelled δ[13]C and benthic foraminifera δ[13]C due to the development of a PMOC (Fig. 1 and Extended Data Fig. 3). Similar to the modern-day Atlantic, the southward flow of the PMOC is concentrated within a western boundary current (western intensification) where there are high δ[13]C values and the eastern return flow has low δ[13]C values. Sites 1209 and 1210 were targeted because they are situated near the western boundary, but owing to their depth, they are not within the core of the modelled PMOC in the simulations. Nonetheless, when isolating the 2,200–2,800 m depth range, the δ[13]C pattern between the data (symbols) and model (contours) largely agrees. That is, Sites 1209 and 1210 have higher δ[13]C values because they are near the western boundary, and Site 1018 has low δ[13]C values owing to the accumulation of respired carbon in the eastern return flow.

Assessing changes in ocean carbon cycle

A modelled increase in ventilation of the deep North Pacific during the mid-Pliocene altered the distribution of ocean carbon globally compared with pre-industrial (Extended Data Figs. 4 and 5). The North Pacific DIC reservoir decreased compared with the pre-industrial control (Extended Data Figs. 6–8)—the deep ocean (>500 m water depth) reservoir decreased by 0.6%, or ~82 PgC, and interestingly, this is counterbalanced by an increase in the surface ocean (<500 m water depth) of 1%, or ~19 PgC. The overall ocean carbon content increased by 1.6% with increases of ~533 PgC (1.6%) and ~57 PgC (1.2%) in the deep and surface ocean, respectively. (For reference, the modern ocean absorbed ~34 Pg of anthropogenic carbon between 1994 and 2007[39].)

The reconfiguration of North Pacific deep ocean circulation probably changed the spatial distribution of nutrient availability throughout the global ocean as evidenced by biogenic opal and alkenone mass accumulation rates[40]. The high latitudes were productive, and there was enhanced export production/preservation, which is particularly evident in the North Pacific, where reduced stratification brought nutrients to the surface and supported opal production/preservation (Fig. 3)[4,41]. Incomplete nutrient utilization[41] in the

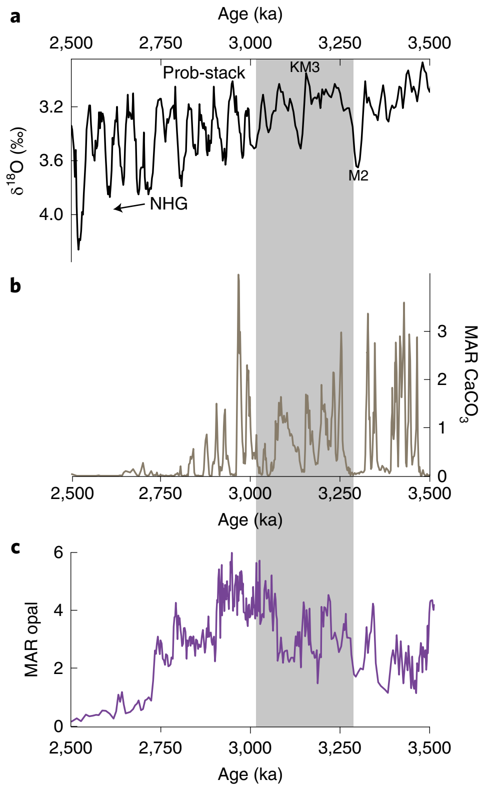

Fig. 3 | Benthic isotope records of Prob-stack and Site 882 sediment records $CaCO_3$ MAR and opal MAR. a, Benthic isotope records of a probabilistic Pliocene-Pleistocene stack (Prob-stack)[45]. **b**,**c**, Site 882 sediment records[41] $CaCO_3$ mass accumulation rate (MAR) (**b**) and opal MAR (**c**).The grey shading indicates the mid-Pliocene Warm Period. Northern Hemisphere glaciation (NHG) and Marine Isotope Stages KM3 and M2 are labelled.

source-water regions of NPDW may have exported excess nutrients to other regions. For example, this Pliocene deep ocean circulation configuration and carbon distribution had knock-on effects and altered biogeochemical cycles in the eastern equatorial Pacific[17] and increased productivity[16]. With the onset of Northern Hemisphere glaciation, the PMOC shut down[4] and North Pacific deep ventilation ceased, as reflected in the $CaCO_3$ (Fig. 3b) and opal accumulation (Fig. 3c) at Site 882[41]). Productivity shifted from high latitudes to lower latitudes during glaciations[40], and deep ocean transport increased between the Pacific and Atlantic basins[42].

An increase in surface ocean DIC may have contributed to the higher-than-pre-industrial CO_2 levels during the mid-Pliocene. High-resolution CO_2 estimates show the average atmospheric CO_2 level was ~360 ppm during the mid-Piacenzian[10]. Higher DIC relative to pre-industrial may have caused a greater CO_2 flux from the ocean to the atmosphere and probably contributed to mid-Pliocene high CO_2.

In summary, the reconstructed carbon isotope gradients, along with isotope-enabled modelling, provide strong support for a major reorganization of the global ocean conveyor belt during the warm Pliocene, with an active PMOC cell having large impacts on Pacific Ocean ventilation and global carbon distribution.

Online content

Any methods, additional references, Nature Research reporting summaries, source data, extended data, supplementary information, acknowledgements, peer review information; details of author contributions and competing interests; and statements of data and code availability are available at https://doi.org/10.1038/s41561-022-00978-3.

Received: 15 September 2020; Accepted: 26 May 2022;
Published online: 14 July 2022

References

1. Pachauri, R. K., M. R. Allen, V. R. Barros, and J. Broome (2014), Climate Change 2014: Synthesis Report. Contribution of Working Groups I, II and III to the Fifth Assessment Report of the Intergovernmental Panel on Climate Change,
2. Rahmstorf, S. Ocean circulation and climate during the past 120,000 years. *Nature* **419**, 207–214 (2002).
3. Warren, B. A. Why is no deep water formed in the North Pacific? *J. Mar. Res.* **41**, 327–347 (1983).
4. Burls, N. J. et al. Active Pacific meridional overturning circulation (PMOC) during the warm Pliocene. *Sci. Adv.* **3**, e1700156 (2017).
5. Kwiek, P. & Ravelo, A. C. Pacific Ocean intermediate and deep water circulation during the Pliocene. *Palaeogeogr. Palaeoclimatol. Palaeoecol.* **154**, 191–217 (1999).
6. McKinley, C. C., Thomas, D. J., LeVay, L. J. & Rolewicz, Z. Nd isotopic structure of the Pacific Ocean 40–10 Ma, and evidence for the reorganization of deep North Pacific Ocean circulation between 36 and 25 Ma. *Earth Planet. Sci. Lett.* **521**, 139–149 (2019).
7. Rae, J. W. et al. Deep water formation in the North Pacific and deglacial CO_2 rise. *Paleoceanography* **29**, 645–667 (2014).
8. Thomas, D. J. Evidence for deep-water production in the North Pacific Ocean during the early Cenozoic warm interval. *Nature* **430**, 65–68 (2004).
9. Haywood, A. M. et al. A return to large-scale features of Pliocene climate: the Pliocene Model Intercomparison Project phase 2. Preprint at *Copernicus* https://doi.org/10.5194/cp-2019-145 (2020).
10. de la Vega, E. et al. Atmospheric CO_2 during the mid-Piacenzian Warm Period and the M2 glaciation. *Sci. Rep.* **10**, 11002 (2020).
11. McClymont, E. L. et al. Lessons from a high-CO_2 world: an ocean view from ~3 million years ago. *Clim. Past* **16**, 1599–1615 (2020).
12. Brierley, C., Burls, N., Ravelo, C. & Fedorov, A. Pliocene warmth and gradients. *Nat. Geosci.* **8**, 419–420 (2015).
13. Burls, N. J. & Fedorov, A. V. What controls the mean east–west sea surface temperature gradient in the equatorial Pacific: the role of cloud albedo. *J. Clim.* **27**, 2757–2778 (2014).
14. Fedorov, A. V., Burls, N.J., Lawrence, K. T. and Peterson, L. C. Tightly linked zonal and meridional sea surface temperature gradients over the past five million years. *Nat. Geosci.* https://doi.org/10.1038/ngeo2577 (2015).
15. Burls, N. J. & Fedorov, A. V. Wetter subtropics in a warmer world: contrasting past and future hydrological cycles. *Proc. Natl Acad. Sci. USA* **28**, 12888–12893 (2017).
16. Lyle, M. & Baldauf, J. Biogenic sediment regimes in the Neogene equatorial Pacific, IODP Site U1338: burial, production, and diatom community. *Palaeogeogr. Palaeoclimatol. Palaeocol.* **433**, 106–128 (2015).
17. Shankle, M. G. et al. Pliocene decoupling of equatorial Pacific temperature and pH gradients. *Nature* **598**, 457–461 (2021).
18. Curry, W. B. & Oppo, D. W. Glacial water mass geometry and the distribution of $\delta^{13}C$ of ΣCO_2 in the western Atlantic Ocean. *Paleoceanogr. Paleoclimatol.* https://doi.org/10.1029/2004PA001021 (2005).
19. Kroopnick, P. M. The distribution of ^{13}C of ΣCO_2 in the world oceans. *Deep Sea Res. A* **32**, 57–84 (1985).
20. Schmittner, A. et al. Calibration of the carbon isotope composition ($\delta^{13}C$) of benthic foraminifera. *Paleoceanogr. Paleoclimatol.* **32**, 512–530 (2017).
21. Gu, S. et al. Assessing the potential capability of reconstructing glacial Atlantic water masses and AMOC using multiple proxies in CESM. *Earth Planet. Sci. Lett.* **541**, 116294 (2020).
22. Lozier, M. S. Deconstructing the conveyor belt. *Science* **328**, 1507–1511 (2010).
23. Jian, Z. et al. Pliocene–Pleistocene stable isotope and paleoceanographic changes in the northern South China Sea. *Palaeogeogr. Palaeoclimatol.* **193**, 425–442 (2003).
24. Mix, A. et al. Benthic foraminifer stable isotope recond from Site 849 (0–5 Ma): local and global climate changes. In *Proc. Ocean Drilling Program, Scientific Results* **138** (eds Pisias, N. G. et al.), 371–412 (1995).
25. Tian, J., Wang, P., Cheng, X. & Li, Q. Astronomically tuned Plio–Pleistocene benthic $\delta^{18}O$ record from South China Sea and Atlantic–Pacific comparison. *Earth Planet. Sci. Lett.* **203**, 1015–1029 (2002).
26. Whitman, J. M. & Berger, W. H. Pliocene–Pleistocene carbon isotope record, Site 586, Ontong Java Plateau. *Mar. Micropaleontol.* **130**, 333–348 (1993).
27. Caballero-Gill, R. P., Herbert, T. D. & Dowsett, H. J. 100-kyr paced climate change in the Pliocene Warm Period, Southwest Pacific. *Paleoceanogr. Paleoclimatol.* **34**, 524–545 (2019).
28. Karas, C. et al. Mid-Pliocene climate change amplified by a switch in Indonesian subsurface throughflow. *Nat. Geosci.* **2**, 434–438 (2009).

29. McClymont, E. L. et al. Pliocene-Pleistocene evolution of sea surface and intermediate water temperatures from the southwest Pacific. *Paleoceanography* **31**, 895–913 (2016).
30. Tiedemann, R., Sturm, A., Steph, S., Lund, S. P. & Stoner, A. J. S. Astronomically calibrated timescales from 6 to 2.5 Ma and benthic isotope stratigraphies, Sites 1236, 1237, 1239, and 1241. In *Proc. Ocean Drilling Program, Scientific Results* **202** (eds Tiedman, R. et al.), 1–69 (2007).
31. Venti, N. L. & Billups, K. Stable-isotope stratigraphy of the Pliocene–Pleistocene climate transition in the northwestern subtropical Pacific. *Palaeogeogr. Palaeoclimatol.* **326-328**, 54–65 (2012).
32. Shackleton, N. J., Hall, M. A. & Pate, D. Pliocene stable isotope stratigraphy of Site 846. In *Proc. Ocean Drilling Program, Scientific Results* **138** (eds Pisias, N. G. et al.), 337–355 (1995).
33. Abell, J. T., Winckler, G., Anderson, R. F. & Herbert, T. D. Poleward and weakened westerlies during Pliocene warmth. *Nature* **589**, 70–75 (2021).
34. Lam R. A. et al. Pliocene to Earliest Pleistocene (5–2.5 Ma) Reconstruction of the Kuroshio Current Extension Reveals a Dynamic Current. https://doi.org/10.1029/2021PA004318 (2021).
35. Venti, N. L., Billups, K. & Herbert, T. D. Paleoproductivity in the northwestern Pacific Ocean during the Pliocene-Pleistocene climate transition (3.0–1.8 Ma) https://doi.org/10.1002/2016PA002955 (2017).
36. Haywood, A. M. et al. Large-scale features of Pliocene climate: results from the Pliocene Model Intercomparison Project. *Climate* **9**, 191–209 (2013).
37. Moore, J. K., Doney, S. C. & Lindsay, K. Upper ocean ecosystem dynamics and iron cycling in a global three-dimensional model. *Global Biogeochem. Cycles* https://doi.org/10.1029/2004GB002220 (2004).
38. Jahn, A. et al. Carbon isotopes in the ocean model of the Community Earth System Model (CESM1). *Geosci. Model Dev.* **8**, 2419–2434 (2015).
39. Gruber, N., Sabine, C. L., Feely, R. A., Key, R. M. & Lee, K. The oceanic sink for anthropogenic CO_2 from 1994 to 2007. *Science* **363**, 1193–1199 (2019).
40. Lawrence, K. T. et al. Time-transgressive North Atlantic productivity changes upon Northern Hemisphere glaciation. *Paleoceanogr. Paleoclimatol.* **28**, 740–751 (2013).
41. Haug, G., Sigman, D., Tiedemann, R., Pedersen, T. & Sarnthein, M. Onset of permanent stratification in the subarctic Pacific Ocean. *Nature* **401**, 779–782 (1999).
42. Woodard, S. C. et al. Antarctic role in Northern Hemisphere glaciation. *Science* **346**, 847–851 (2014).
43. Patterson, M. O. et al. A Southwest Pacific perspective on long-term global trends in Pliocene–Pleistocene stable isotope records. *Paleoceanogr. Paleoclimatol.* **33**, 825–839 (2018).
44. Woodhouse, A. et al. Adaptive ecological niche migration does not negate extinction susceptibility. *Sci. Rep.* **11**, 15411 (2021).
45. Ahn, S., Khider, D., Lisiecki, L. E. & Lawrence, C. E. A probabilistic Pliocene–Pleistocene stack of benthic $\delta^{18}O$ using a profile hidden Markov model. *Dyn. Stat. Clim. Syst.* **2**, 91–16 (2017).

Publisher's note Springer Nature remains neutral with regard to jurisdictional claims in published maps and institutional affiliations.

Methods

Site locations. The ODP Sites 1209 (32° 39.1001′ N, 158° 30.3560′ E, 2,698 m water depth) and 1210 (32° 13.4123′ N, 158° 15.5618′ E, 2,585 m water depth) are located on the Shatsky Rise in the Northwest Pacific Ocean. Few sites in the Northwest Pacific Ocean have been drilled by the International Ocean Discovery Program; these sites on the Shatsky Rise are the only sites proximal to the modelled NPDW with the foraminifera preservation necessary for stable isotope reconstructions during the Pliocene.

Sample preparation and stable isotope analyses. Sediment samples were washed and picked for the benthic foraminifera *Cibicidoides wuellerstorfi* (>150 µm size fraction). Approximately 3–5 foraminifera were analysed for oxygen and carbon-stable isotope analyses on the VG ISOGAS SIRA dual inlet isotope ratio mass spectrometer in the Godwin Laboratory for Palaeoclimate Research at the University of Cambridge. Long-term analytical reproducibility for NBS-19 is ±0.06 and 0.05 (1 s.d.) for carbon and oxygen isotopes, respectively.

Age model. Orbitally tuned age models for Sites 1209 and 1210 were constructed using HMM-Stack[46,47] to align the benthic oxygen isotope records with Prob-stack[45], which is an updated version of LR04[48]. Sampling resolution is one sample every ~3.8 kyr and ~5.2 kyr for Sites 1209 and 1210, respectively.

Calculating Pliocene to core tops and pre-industrial water-column $\delta^{13}C$ anomalies. To calculate a $\delta^{13}C$ anomaly from pre-industrial for the mid- and early Pliocene we used the OC3 database[20]. The OC3 database includes pre-industrial $\delta^{13}C$ natural ocean water-column bottle data and late Holocene $\delta^{13}C$ from the benthic foraminifera genus *Cibicides* (without species-specific adjustments). We used the OC3's horizontal great-circle distance (Δd) and the vertical distance (Δz) search options to identify pre-industrial samples closest to the drilled site locations. We started with OC3's 'conservative' option ($\Delta d = 500$ km, $\Delta z = z/10$) and expanded to OC3's 'liberal' option ($\Delta d = 1{,}000$ km, $\Delta z = z/5$) as necessary. In some instances, it was necessary to widen the great-circle distance further (Table 1). The published Pliocene $\delta^{13}C$ values were adjusted using species-specific corrections (*Uvigerina* spp. were adjusted by 0.90‰ after ref. [49]). The anomaly was calculated by subtracting pre-industrial OC3 $\delta^{13}C$ estimates from the mid- and early Pliocene $\delta^{13}C$ values (Pliocene – pre-industrial).

Modelling methods. Three fully coupled simulations, referred to as the pre-industrial control, mid-Pliocene-like (mid-Piacenzian) and early Pliocene-like experiments were performed using the CESM v.1.2.2. All simulations were run with active biogeochemistry[37] and carbon isotopes[38]. Given the multi-millennial timescale over which the deep ocean and biogeochemical cycles equilibrate, and the computational cost associated with running a fully coupled climate model with numerous tracers in the ocean component, a CESM version with a relatively low horizontal resolution and the Community Atmosphere Model, Version 4, as the atmospheric component (also referred to as CCSM4) is used. This CESM configuration has atmosphere and land components on a T31 spectral grid (horizontal grid of 3.75° × 3.75°) while the ocean and sea-ice components employ a tripolar grid with a resolution that ranges from 3° near the poles to 1° near the Equator (see ref. [50] for further details). Each simulation was initialized from modern ocean conditions and run for 3,000 years.

The pre-industrial simulation was run using the default 'B_1850_BGC-BDRD' component set in which atmospheric CO_2 is set at 284.7 ppmv. The only exception to the default set-up was the inclusion of the carbon isotope code in which atmospheric $\delta^{13}C$ values are set to −6.379. Spatial warming patterns resembling reconstructed mid- and early Pliocene warming patterns (Extended Data Fig. 2) were obtained by changing the meridional cloud albedo gradient within these experiments. For the early Pliocene-like experiment, the liquid water path was reduced polewards of 15° N and 15° S by 60% while the ice and liquid water paths were increased equatorwards of 15° N and 15° S by 240%, but only in the short-wave radiation scheme. These changes act to increase cloud albedo in the tropics and reduce it in the extra tropics; the exact percentage by which the liquid water path and ice water path are scaled correspond to experiment 16 in ref. [13]. A more detailed analysis of the applicability of this experimental design to early Pliocene conditions is detailed in ref. [51]; also see the method section of ref. [4] for an in-depth discussion of the framework and previous literature motivating this approach. This simply reproduces the changes in the meridional structure of net cloud radiative forcing required to reproduce Pliocene warming patterns rather than the exact mechanism that could have occurred via short wave, long wave or both. These radiative forcing changes may have been realized by changes in a number of cloud properties in addition to liquid and ice water content and sustained by different Pliocene atmospheric aerosol concentrations or unresolved cloud feedbacks to elevated CO_2 levels during the Pliocene. The appeal of this approach is that the warming patterns are largely reproduced and their impact on the hydrological cycle and surface buoyancy gradient that affect the meridional overturning circulation simulated. Note that while in the early Pliocene-like experiment CO_2 was set to 280 ppm in the atmospheric component (the global warming is supported instead by the cloud albedo changes and the feedbacks that they invoke), atmospheric CO_2 was set to 400 ppm for the ocean biogeochemistry and carbon isotope components. Using pre-industrial values of CO_2 in the atmospheric model is justified because the imposed modifications in cloud radiative properties dominate the simulated climatic changes. Likewise, modern palaeogeography was used for all three experiments, as potential changes in, for example, ocean throughways would have very minor effects in comparison (for example, ref. [52]). For the mid-Pliocene-like experiment, to achieve the more modest reduction of the large-scale SST gradients suggested by the proxy data, the liquid water path was reduced poleward of 15° N and 15° S by 50% and the ice and liquid water paths were increased equatorwards of 15° N and 15° S by 240% while atmospheric CO_2 was set to 400 ppm in an attempt to be more physically consistent (as mentioned, in reality, Pliocene warmth was probably maintained by elevated Pliocene CO_2 levels with the imposed cloud radiative forcing changes resulting from unresolved cloud feedbacks to the elevated CO_2 levels or different Pliocene atmospheric aerosol concentrations or some combination of both).

SST reconstruction for model comparison. Here we use the published alkenone records[14,29,53–67] to compare proxy SST with the mid-Pliocene (mid-Piacenzian, 3.264–3.025 Ma) and early Pliocene (4–5 Ma) model output. Alkenone SST estimates (Extended Data Fig. 2) are in diamonds[68] and squares[69], and the anomalies calculated from the core-top and pre-industrial estimates are from ref. [70] (and references within) and ref. [61]. In general, the proxy and model output show high-latitude amplification and warm upwelling regions during the Pliocene compared with today.

Data availability

The stable isotope data generated here for Shatsky Rise and those compiled for the spatial analyses are available at figshare (DOI: 10.6084/m9.figshare.20233857) and will also be available on Pangaea.de.

Code availability

The CESM 1.2.2.1 code used to run the climate simulations is available from https://svn-ccsm-models.cgd.ucar.edu/cesm1/release_tags/cesm1_2_2_1. The code modifications made to CESM 1.2.2.1 to include carbon isotopes following ref. [38] are available from https://github.com/nburls/FordEtAl2022_CISOmods. Figures with coastal outlines (for example, Figs. 1 and 2 and Extended Data Figs. 1 and 2) were created in Matlab with the M_maps package[71].

References

46. Butcher, S., King, T. & Zalewski, L. *Apocrita—High Performance Computing Cluster for Queen Mary University of London* (2017).
47. Lin, L., Khider, D., Lisiecki, L. E. & Lawrence, C. E. Probabilistic sequence alignment of stratigraphic records. *Paleoceanogr. Paleoclimatol.* **29**, 976–989 (2014).
48. Lisiecki, L. E. & Raymo, M. E. A Pliocene–Pleistocene stack of 57 globally distributed benthic $\delta^{18}O$ records. *Paleoceanogr. Paleoclimatol.* **20**, PA1003 (2005).
49. Duplessy, J. C. et al. 13C record of benthic foraminifera in the last interglacial ocean: implications for the carbon cycle and the global deep water circulation. Quat. Res. https://doi.org/10.1016/0033-5894(84)90099-1 (1984).
50. Shields, C. A. et al. The low-resolution CCSM4. *J. Clim.* **25**, 3993–4014 (2012).
51. Burls, N. J. & Fedorov, A. V. Simulating Pliocene warmth and a permanent El Niño-like state: the role of cloud albedo. *Paleoceanogr. Paleoclimatol.* **29**, 893–910 (2014).
52. Brierley, C. M. & Fedorov, A. V. Comparing the impacts of Miocene–Pliocene changes in inter-ocean gateways on climate: Central American Seaway, Bering Strait, and Indonesia. *Earth Planet. Sci. Lett.* **444**, 116–130 (2016).
53. bin Shaari, H., Yamamoto, M. & Irino, T. Enhanced upwelling in the eastern equatorial Pacific at the last five glacial terminations. *Paleogeogr. Paleoclimatol.* **386**, 8–15 (2013).
54. Brierley, C. M. et al. Greatly expanded tropical warm pool and weakened Hadley circulation in the early Pliocene. *Science* **323**, 1714–1718 (2009).
55. Dekens, P. S., Ravelo, A. C. & McCarthy, M. D. Warm upwelling regions in the Pliocene Warm Period. *Paleoceanogr. Paleoclimatol.* **22**, PA3211 (2007).
56. Etourneau, J., Schneider, R., Blanz, T. & Martinez, P. Intensification of the Walker and Hadley atmospheric circulations during the Pliocene–Pleistocene climate transition. *Earth Planet. Sci. Lett.* **297**, 103–110 (2010).
57. Herbert, T. D. et al. Late Miocene global cooling and the rise of modern ecosystems. *Nat. Geosci.* https://doi.org/10.1038/ngeo2813 (2016).
58. LaRiviere, J. P. et al. Late Miocene decoupling of oceanic warmth and atmospheric carbon dioxide forcing. *Nature* **486**, 97–100 (2012).
59. Lawrence, K. T., Liu, Z. & Herbert, T. D. Evolution of the eastern tropical Pacific through Plio-Pleistocene glaciation. *Science* **312**, 79–83 (2006).
60. Li, L. et al. A 4-Ma record of thermal evolution in the tropical western Pacific and its implications on climate change. *Earth Planet. Sci. Lett.* **309**, 10–20 (2011).
61. Liu, J. et al. Eastern equatorial Pacific cold tongue evolution since the late Miocene linked to extratropical climate. *Sci. Adv.* **5**, eaau6060 (2019).
62. Martinez-Garcia, A., Rosell-Mele, A., McClymont, E. L., Gersonde, R. & Haug, G. H. Subpolar link to the emergence of the modern equatorial Pacific cold tongue. *Science* **328**, 1550–1553 (2010).

63. O'Brien, C. L. et al. High sea surface temperatures in tropical warm pools during the Pliocene. Nat. Geosci. https://doi.org/10.1038/ngeo2194 (2014).
64. Pagani, M., Liu, Z., LaRiviere, J. & Ravelo, A. C. High Earth-system climate sensitivity determined from Pliocene carbon dioxide concentrations. *Nat. Geosci.* **3**, 27–30 (2010).
65. Rousselle, G., Beltran, C., Sicre, M.-A., Raffi, I. & De Rafélis, M. Changes in sea-surface conditions in the equatorial Pacific during the middle Miocene–Pliocene as inferred from coccolith geochemistry. *Earth Planet. Sci. Lett.* **361**, 412–421 (2013).
66. Seki, O. et al. Paleoceanographic changes in the eastern equatorial Pacific over the last 10 Myr. *Paleoceanogr. Paleoclimatol.* https://doi.org/10.1029/2011PA002158 (2012).
67. Zhang, Y. G., Pagani, M. & Liu, Z. A 12-million-year temperature history of the tropical Pacific Ocean. *Science* **344**, 84–87 (2014).
68. Tierney, J. E. & Tingley, M. P. BAYSPLINE: a new calibration for the alkenone paleothermometer. *Paleoceanogr. Paleoclimatol.* **33**, 281–301 (2018).
69. Müller, P. J., Kirst, G., Ruhland, G., von Storch, I. & Rosell-Mele, A. Calibration of the alkenone paleotemperature index $U_{37}^{K'}$ based on core-tops from the eastern South Atlantic and the global ocean (60° N–60° S). *Geochim. Cosmochim. Acta* **62**, 1757–1772 (1998).
70. Tierney, J. E., Haywood, A. M., Feng, R., Bhattacharya, T. & Otto-Bliesner, B. L. Pliocene warmth consistent with greenhouse gas forcing. *Geophys. Res. Lett.* **46**, 9136–9144 (2019).
71. Pawlowicz, R. M_Map: A mapping package for MATLAB v.1.4m (2020); www.eoas.ubc.ca/~rich/map.html

Acknowledgements

We thank J. Booth, J. Rolfe and J. Nicolson for their laboratory assistance and the International Ocean Discovery Program core repository for providing samples. This work benefited from conversations with L. Haynes and M. Lyle. We acknowledge high-performance computing support from Cheyenne (https://doi.org/10.5065/D6RX99HX) provided by NCAR's Computational and Information Systems Laboratory, sponsored by the NSF. This work was supported by Natural Environment Research Council (NE/N015045/1; H.L.F.), the National Science Foundation (OCE-1844380 and OCE-2002448; N.J.B.) and a Sloan Ocean Fellowship (N.J.B.). H.L.F. personally thanks the breast cancer oncology, chemotherapy, radiotherapy and surgical team at St Bartholomew's Hospital.

Author contributions

H.L.F. and N.J.B. designed, analysed and interpreted the data. P.J. contributed to the numerical simulations and carbon budget analyses. H.L.F. wrote the manuscript with contributions from N.J.B.; H.L.F., N.J.B., P.J., A.J., R.P.C.-G., D.A.H. and A.V.F. contributed to the manuscript and the revisions.

Competing interests

The authors declare no competing interests.

Additional information

Extended data is available for this paper at https://doi.org/10.1038/s41561-022-00978-3.

Supplementary information The online version contains supplementary material available at https://doi.org/10.1038/s41561-022-00978-3.

Correspondence and requests for materials should be addressed to H. L. Ford.

Peer review information *Nature Geoscience* thanks Claire McKinley and the other, anonymous, reviewer(s) for their contribution to the peer review of this work. Primary Handling Editor: James Super, in collaboration with the *Nature Geoscience* team.

Reprints and permissions information is available at www.nature.com/reprints.

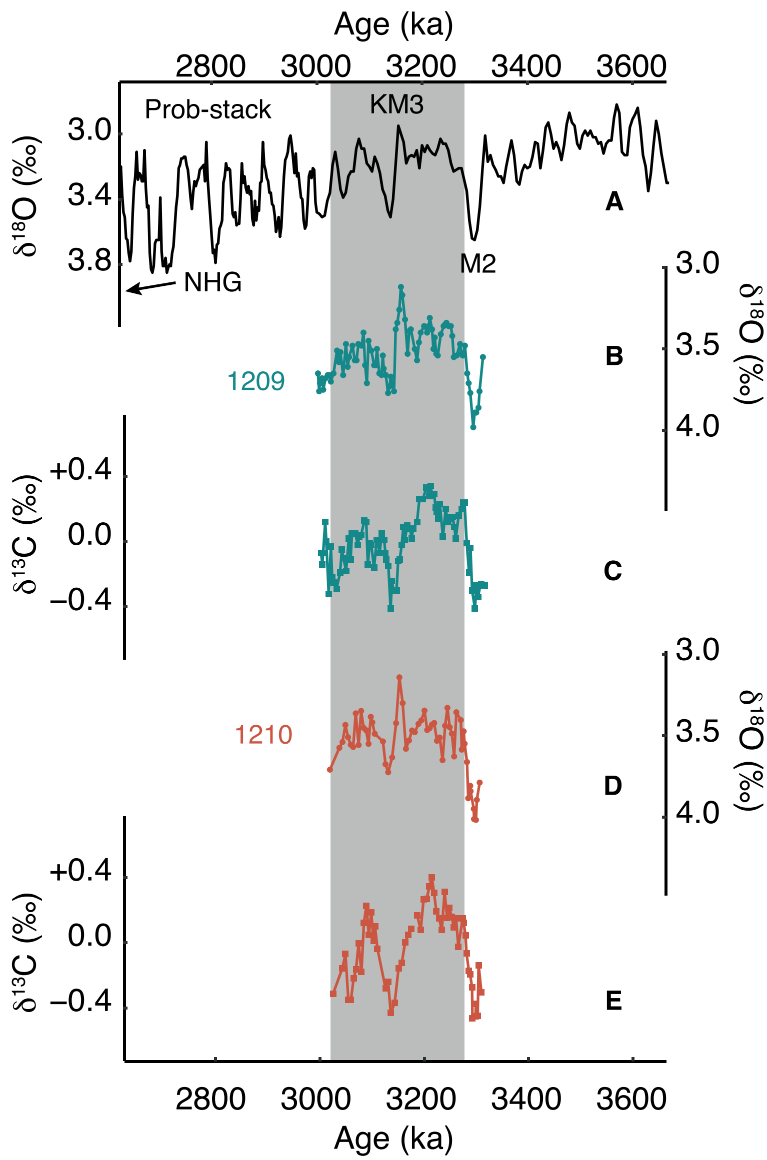

Extended Data Fig. 1 | Global benthic foraminifera oxygen isotope stack and North Pacific records. Benthic isotope records of Prob-stack (A[45]), Site 1209 $\delta^{18}O$ (B, blue circles) and $\delta^{13}C$ (C, blue squares), and Site 1210 $\delta^{18}O$ (D, orange circles) and $\delta^{13}C$ (E, orange squares). The grey shading indicates the mid-Piacenzian warm period. Northern Hemisphere Glaciation (NHG) and Marine Isotope Stages KM3 and M2 are labelled.

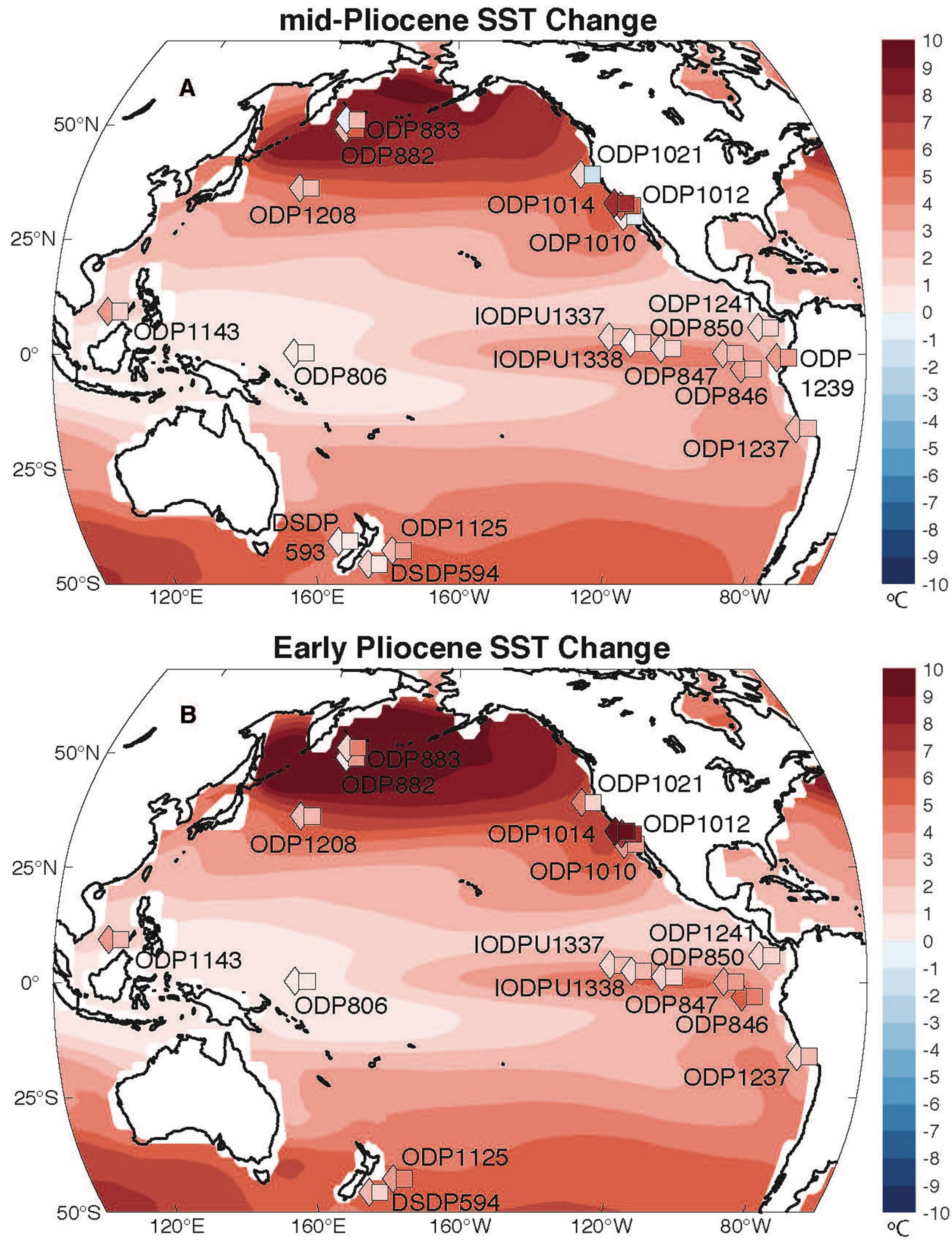

Extended Data Fig. 2 | Pliocene sea surface temperature records. Sea surface temperature (SST) anomaly maps for the mid-Pliocene Warm Period (mid-Piacenzian 3.264–3.025 Ma) and Early Pliocene (4–5 Ma).

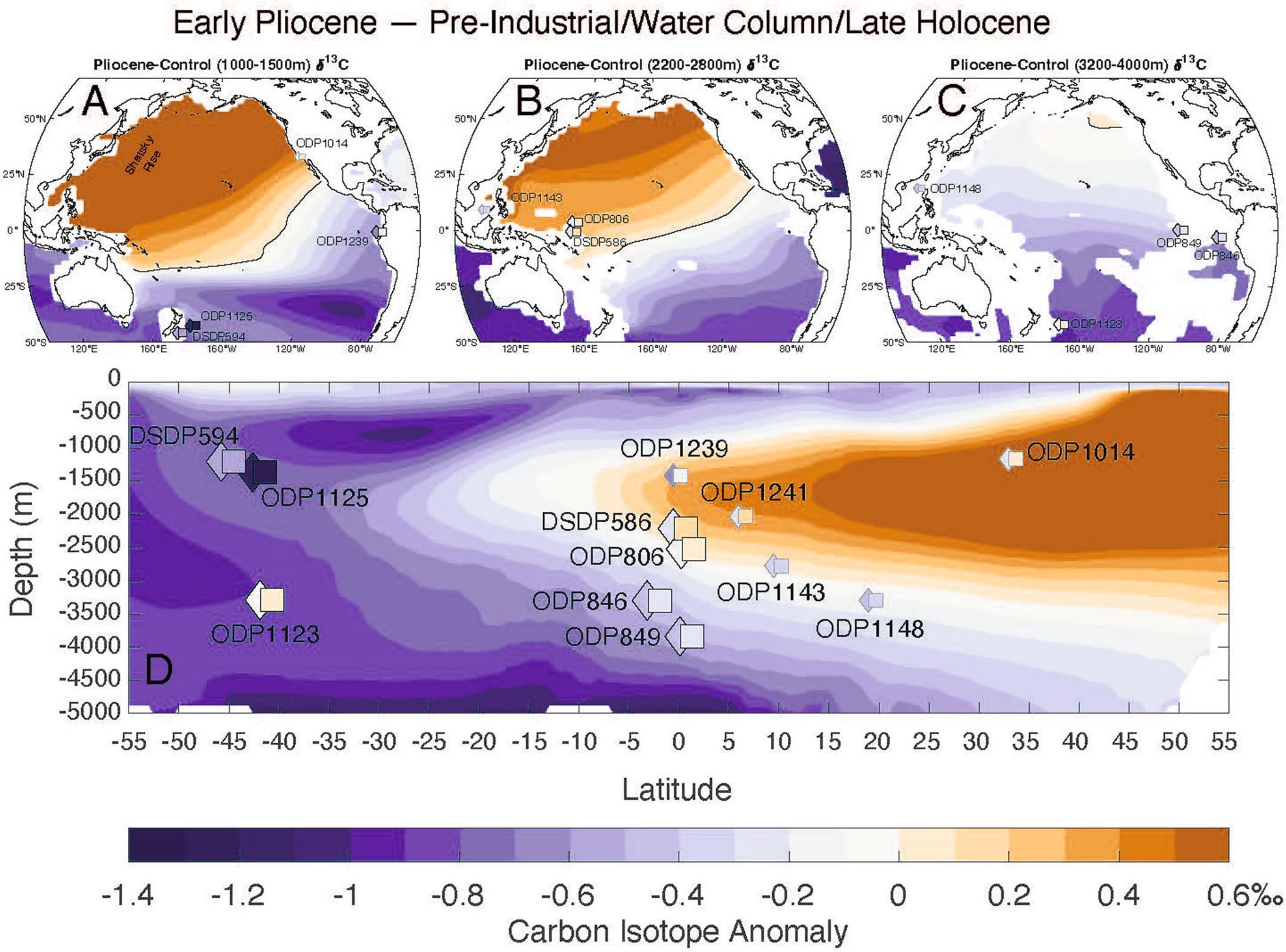

Extended Data Fig. 3 | Early Pliocene δ^{13}C anomaly maps for the Pacific Ocean. Observed benthic δ^{13}C and modelled zonal-mean (shaded contours in ‰) anomalies for the Early Pliocene (4–5 Ma). The benthic δ^{13}C anomaly (‰) is calculated from the OC3 database[20] with Late Holocene core top (diamonds) and modern δ^{13}C ocean water (squares) values. Large symbols for open ocean sites are outlined in black, while symbols for marginal sites possibly influenced by boundary effects are small and outlined in grey. Horizontal basin-wide δ^{13}C anomalies for 1000–1500 m (A), 2200–2800 m (B), and 3200–4000 m (C) water depth. The largest anomaly is found in the west due to western intensification of deep ocean circulation. The vertical cross section across the Pacific (D) shows the core and spatial extent of the PMOC.

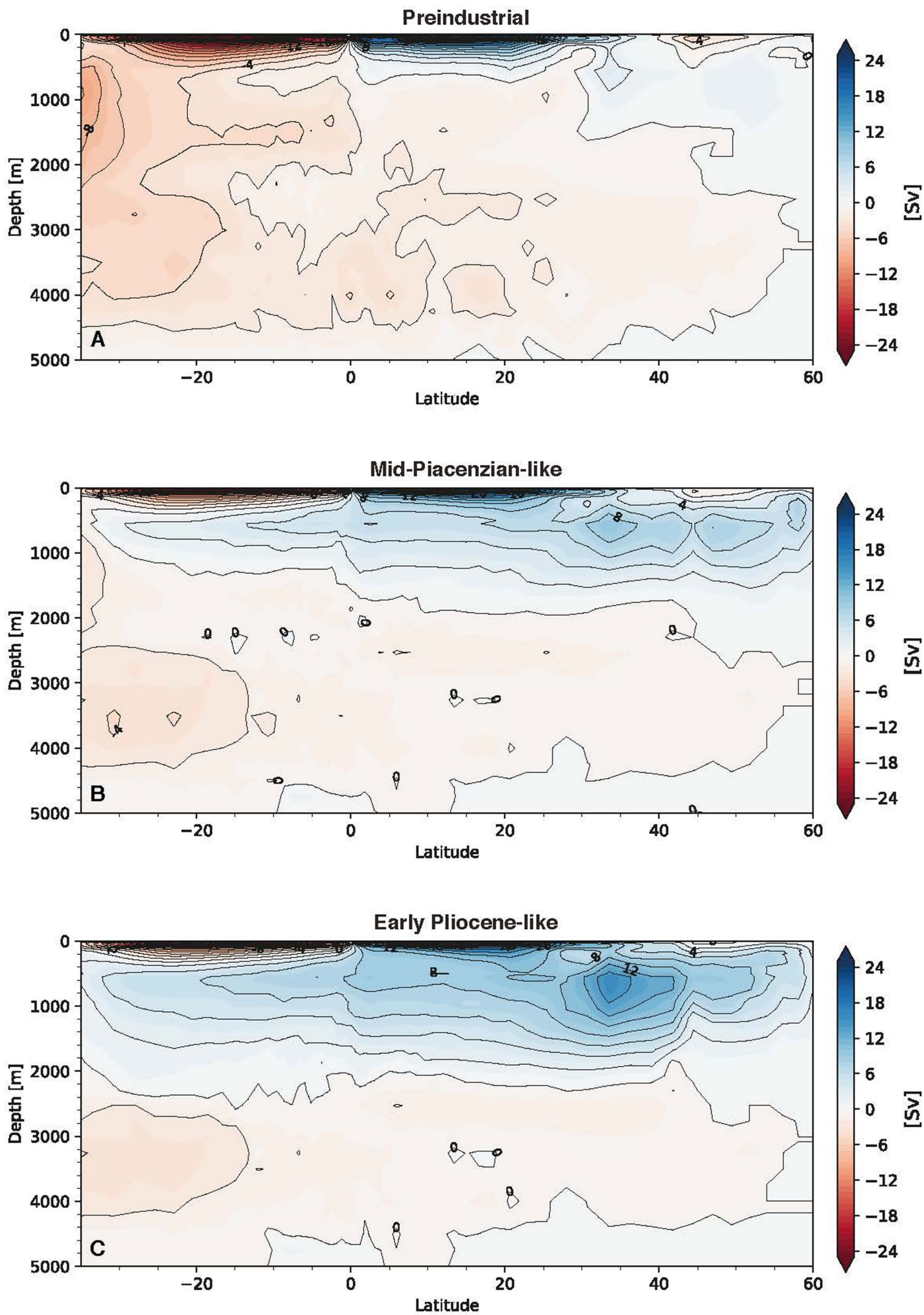

Extended Data Fig. 4 | Meridional overturning circulation in the Indo-Pacific Ocean. Meridional overturning stream function in the Indo-Pacific ocean (in Sverdup, Sv) for the Pre-industrial (A), mid-Pliocene-like (mid-Piacenzian) (B), and Early Pliocene (C) model simulations. Contour interval is 2 Sv. Note the absence of active overturning cells in the preindustrial simulation other than the upper-ocean wind-driven cells.

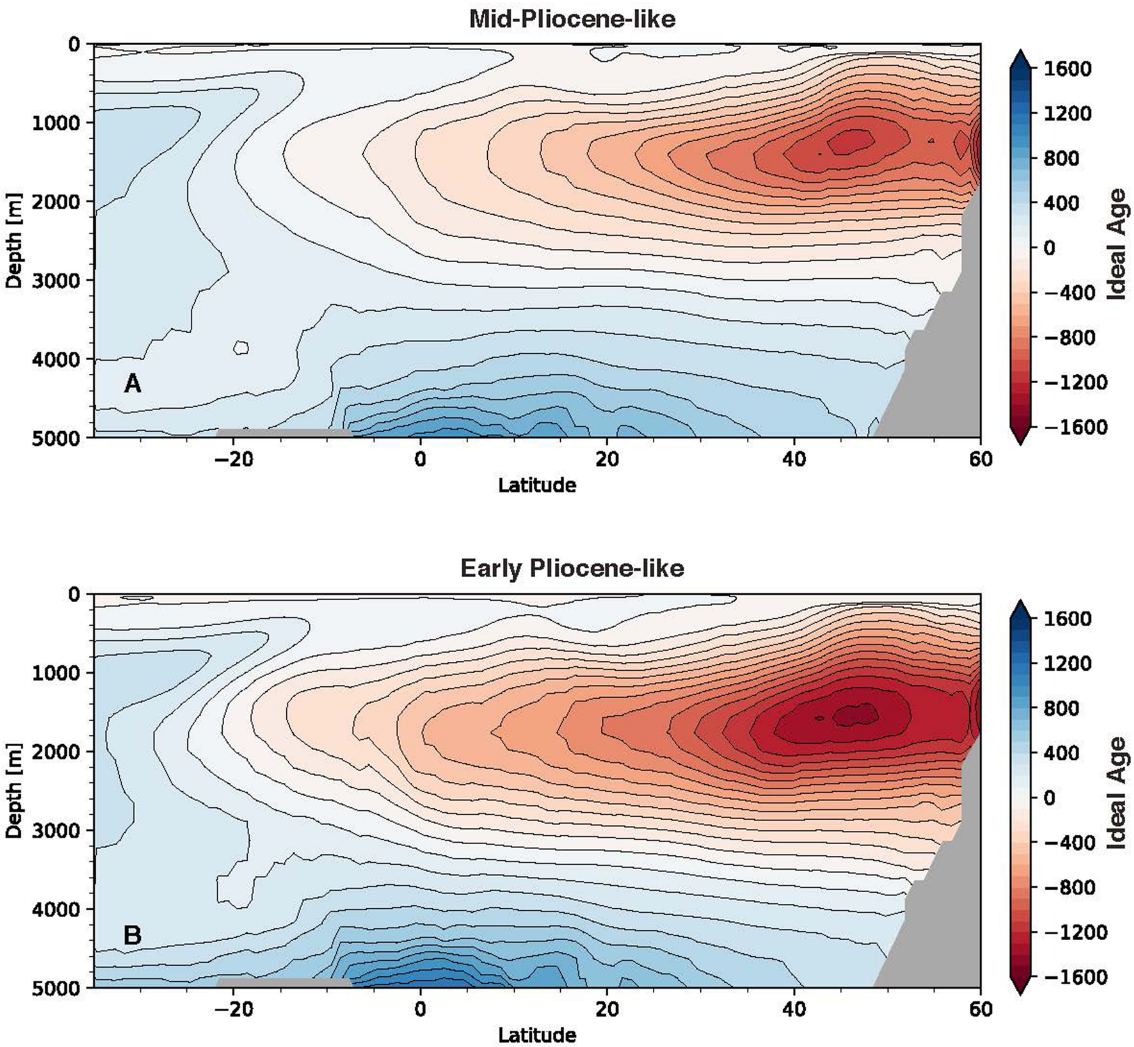

Extended Data Fig. 5 | Meridional ideal age for in Indo-Pacific Ocean. Meridional ideal age in the Indo-Pacific ocean for the mid-Pliocene-like (mid-Piacenzian) (A), and Early Pliocene (B) model simulations minus Pre-industrial. Contour interval is 100 ideal years.

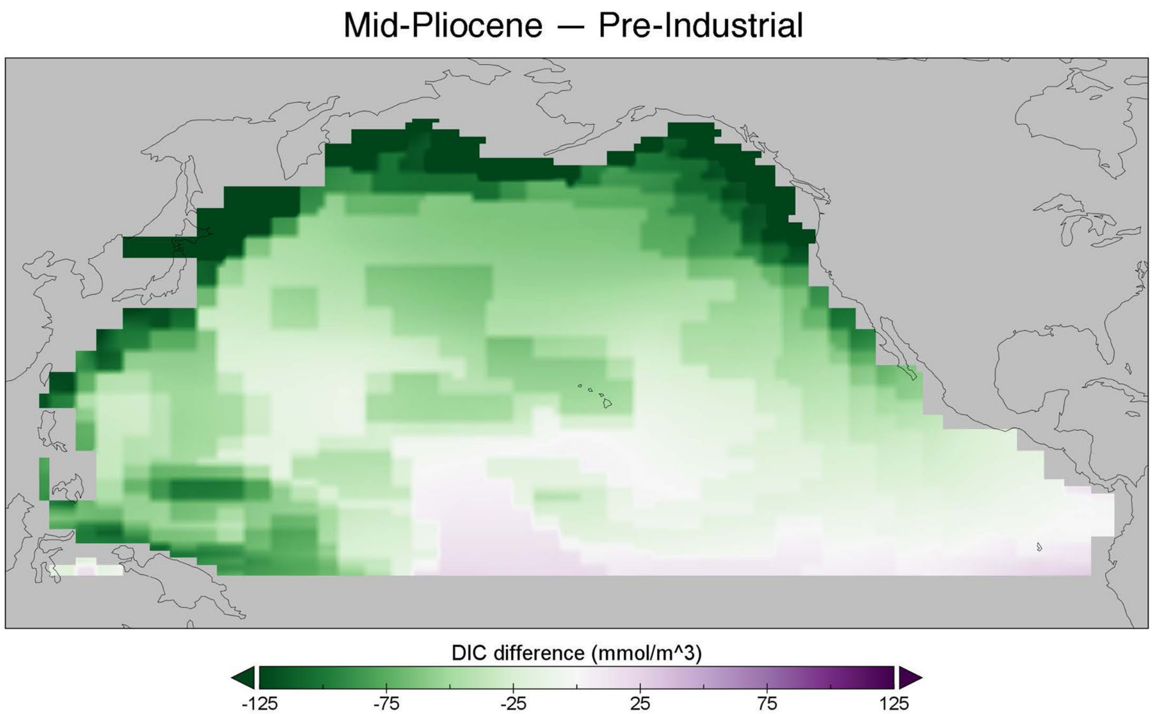

Extended Data Fig. 6 | Modelled DIC anomaly for the Pacific Ocean basin. Pacific basin modelled DIC anomaly from the Pre-Industrial to the mid-Pliocene-like simulation.

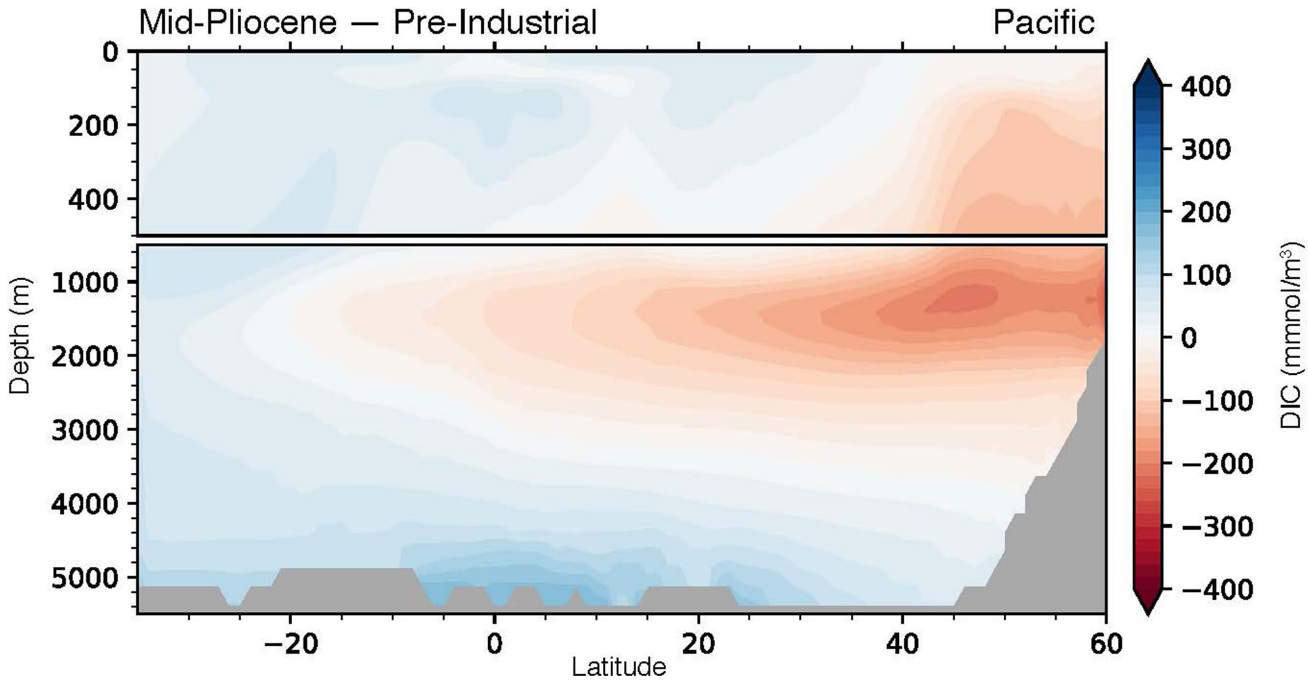

Extended Data Fig. 7 | Modelled zonal mean DIC anomaly for the Pacific Ocean. Pacific basin modelled zonal mean DIC anomaly from the Pre-Industrial to the mid-Pliocene-like simulation.

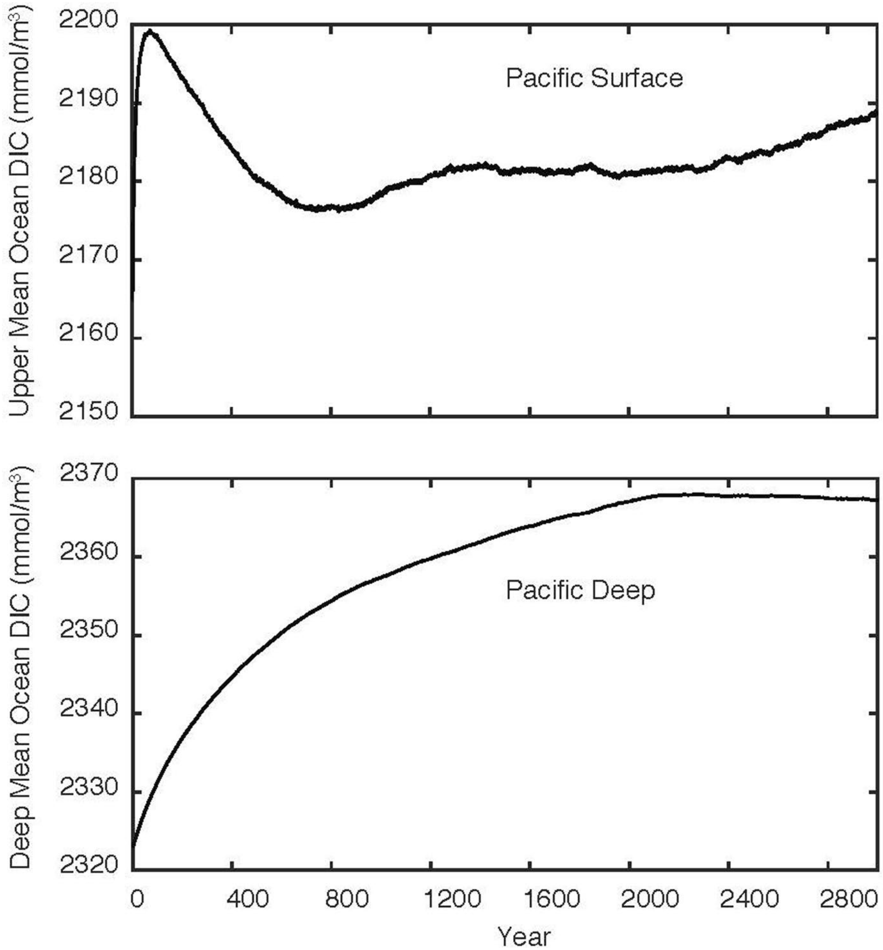

Extended Data Fig. 8 | Model run age and DIC anomaly. Time series of modelled DIC anomaly from the Pre-Industrial to the mid-Pliocene-like simulation. Deep ocean is near equilibrium at ~2000 model run years.